npj | Materials Degradation

www.nature.com/npjmatdeg

ARTICLE OPEN

Check for updates

Comparative structural investigations of nuclear waste glass alteration layers and sol-gel synthesized aerogels

Joelle T. Reiser[1,2], Joseph V. Ryan[2]✉, Marc H. Weber[3], Jan Ilavsky[4], Matthew J. Olszta[2], Daniel K. Schreiber[2] and Nathalie A. Wall[1]

While various glass alteration layer formation mechanisms have been debated in recent years, the glass alteration community generally agrees that more information on physical properties of the alteration layers is needed to further the understanding of their impacts on overall glass alteration. In this work, pore volumes and solid structures of glass (International Simple Glass, ISG) alteration layers formed in solutions of various pH conditions in initially dilute conditions at 90 °C are evaluated with positron annihilation spectroscopy, small-angle X-ray scattering, and scanning transmission electron microscopy. Pore volumes of alteration layers formed at pH 9 were found to be at their lowest near the surfaces of the alteration layers. Solid structures of alteration layers are compared with those of synthetic aerogels of comparable compositions produced under various pH conditions. Alteration layers formed at pH 11 on ISG were shown to contain large structures (>10 nm) similar to synthetic aerogels created under neutral and basic conditions whereas alteration layers formed at pH 9 did not. Available dissolved silica species defined by silica solubility were proposed to have the greatest impact on alteration layer structure.

npj Materials Degradation (2020)4:5 ; https://doi.org/10.1038/s41529-020-0109-y

INTRODUCTION

While commercial nuclear reactors provide reliable energy, resulting wastes require safe disposal to ensure the safety of humans and the environment. Vitrification is one of the current methods for immobilizing nuclear wastes in glass.[1,2] When exposed to aqueous solutions, borosilicate glasses are altered through several possible processes including ion exchange of solution ions (e.g., H_3O^+) with mobile glass ions (e.g., Na^+, Li^+, K^+), hydrolysis/congruent dissolution of the glass network, and the formation of alteration products such as a porous alteration gel layer at the surface of glasses.[3–12]

The general mechanisms of the formation of alteration layers and their role in long-term glass alteration are still being debated.[9,11,13,14] In an inter-diffusion model, ion exchange processes cause solution conditions to be more favorable for hydrolysis by increasing the pH. The alteration layer results from condensation reactions of mostly silicon-based hydrolyzed species from the glass that did not necessarily break every covalent bond from the original glass.[13,15,16] In contrast, another mechanistic model proposes a congruent glass dissolution resulting in the alteration layer being composed entirely of species (primarily Si) that have been completely disassociated from the original glass (dissolution/precipitation).[11,17,18] As a result, an alteration layer composed of spherical silica aggregates of variable sizes and porosities forms. Since the alteration layer is generated from completely free silica species in solution, the proposed model is similar to what is observed in other silica–water systems.[11,18,19] Silica–water systems include sol-gel synthesized silica gels, which have formation mechanisms similar to what Geisler et al. proposed for alteration layers.[11,20]

Sol-gel synthesized silica gels are typically prepared by mixing silicon alkoxides, like tetraethyl orthosilicate (TEOS), with water in a mutual solvent (such as ethanol) in which hydrolysis and polycondensation reactions occur.[19–22] Hydrolysis is limited by the amount of available water molecules, and condensation reactions between two silanol groups or a silanol group and ethoxy group occur to form bridging oxygens or siloxane groups, i.e., Si–O–Si. Continuation of hydrolysis and condensation reactions form colloidal particles (sol) that link into gels over time.

In silica–water systems, several variables impact the polymerization behavior, primarily pH and the presence of background salts, which influence pore and particle sizes of the final gel.[19,20,23,24] Multiple polymerization processes, specifically Ostwald ripening and aggregation, contribute to the formation of large silica networks where the predominance of various processes varies with pH. Ostwald ripening refers to the growth of large individual particles at the expense of small particles mostly via hydrolysis/condensation reactions. Aggregation refers to multiple particles connecting (usually electrostatically) which can then undergo condensation reactions to connect to one another and form a gel. Aggregation occurs preferentially in pH regimes near the isoelectric point, but the size of the particles that aggregate is often influenced by the extent of Ostwald ripening that has previously occured.[19] At low pH, silica colloids have little surface charge, hence they are able to collide and aggregate into chains that eventually form into gel networks. At higher pH (>7) and in the absence of salts or catalysts, silica colloids are repelled by their large negative surface charge. As a result, collisions and aggregation do not readily occur. Instead, the smallest colloids are consumed through Ostwald ripening processes to produce much larger silicate particles.[19,25] Eventually, the dimensions of the Si particles increase to a point where they aggregate with one another since the charge repulsions between individual particles have been greatly reduced per unit area. In addition, increased salt concentrations (>0.2 N at room temperature) lead to the formation of double electrostatic layers by cation counter-ions on negatively charged silicate species, leading to reduced electrostatic repulsion and conditions that allow for more collisions and

[1]Washington State University, Chemistry Department, Pullman, WA 99164, USA. [2]Pacific Northwest National Laboratory, Energy and Environment Directorate, Richland, WA 99352, USA. [3]Washington State University, Center for Materials Research, Pullman, WA 99164, USA. [4]Argonne National Laboratory, X-ray Science Division, Advanced Photon Source, Argonne, IL 60439, USA. ✉email: joe.ryan@pnnl.gov

Published in partnership with CSCP and USTB

npj nature partner journals

increased aggregation even at high pH.[19,20] Final gels prepared in acidic conditions generally consist of linear chains that entangle and form additional branches, whereas final gels in basic conditions form through highly branched clusters that link to create the gel network.[19,20,22,26–28] As a result, gels synthesized in acidic conditions contain smaller pores and are composed of smaller particles than those prepared under basic conditions.

Although the hydrolysis and condensation reactions are similar to those proposed for alteration layer formation for both inter-diffusion and dissolution/precipitation models, the starting silica species differ, whereas the dissolution/precipitation model presents initial silica species similar to those formed during sol-gel synthesis. By examining physical properties of synthetic aerogels and glass alteration layers created at 90 °C for 7 days in static conditions under various pH conditions (buffered solutions), comparisons can be made between aerogels that are known to be created completely from free silica species through sol-gel synthesis with alteration layers formed from glass alteration. This work was conducted using International Simple Glass (ISG), designed and fabricated by the international nuclear waste glass community to unify research efforts in understanding glass properties and durability behavior.[3] ISG has been intensively researched by the international community using multiple methods for various purposes as seen in these cited examples and in the web collection on ISG associated with *npj Materials Degradation* (https://www.nature.com/collections/wwcfskftrj).[14,29–37]

RESULTS

Glass alteration solution and SEM analyses

Table 1 shows the buffered reaction solution pH (90 °C) before and after the alteration experiments. The alteration experiment samples are identified by a three character code (XXX), where the first character represents the target pH of the reactant solution (3, 5, 7, 9, 11), the second character refers to the glass used (I for ISG), and the third denotes the experiment duration in days (7). As an example, ISG altered for 7 days in pH 3 solution, the sample is denoted as 3I7. Over the course of the 7-day experiment, the pH of each solution increases, implying elemental release from the glass exceeded the capacities of the buffers. The solutions originally buffered to pH 3 and pH 5 increased more significantly likely due to the preferable release of alkali glass cations (Na) into solution at low pH as seen previously.[38] Since the pH fluctuated throughout the experiments, the alteration layers evolved in a dynamic solution pH environment rather than an anticipated static one.

Figure 1 illustrates scanning electron microscope backscattered electron (BSE SEM) micrographs of cross-sectioned samples of (a) 3I7, (b) 5I7, (c) 7I7, and (d) 9I7. In addition, two SEM micrographs of 11I7 are shown in Fig. 1 including (e) 11I7a, which shows a small conformal alteration layer (AL) visible in the majority (>50%) of the surface analyzed, and (f) 11I7b, which shows large fragile alteration products in addition to the small AL in the minority (<50%) of surface analyzed. The discrepancy between the ALs observed on 11I7 in Fig. 1e, f could be due to the loss of large fragile alteration products during sample handing and preparation. As pH of the solutions increase, interfaces between unaltered glass (UG) and ALs become irregular, and the ALs are more non-uniform in thickness and appearance. Figure 1 also provides a graphical comparison of calculated equivalent thickness (ETh_B) calculated in Kaspar et al. using boron concentrations obtained from ICP-OES analysis and measured thicknesses from SEM micrographs of the altered portions of 3I7, 5I7, 7I7, 9I7, and 11I7.[39] (See Supplementary Table 3 for ETh_B and measured thickness values.) The trend of alteration layer thickness as a function of pH observed in Fig. 1 is consistent with the observations from high flow experiments compiled by Strachan.[40–43] These works showed glass dissolution has a V- or U-shape dependence on pH where glass altered at neutral pH would alter less than glass altered at low and high pH conditions.

Table 1. Initial and final $pH_{90\,°C}$ of solutions used for glass dissolution.

Sample	Initial $pH_{90\,°C}$	Final $pH_{90\,°C}$
3I7	3.00	5.27
5I7	5.09	6.49
7I7	7.16	7.45
9I7	8.99	9.23
11I7	11.10	11.34

This table can also be found in Kaspar et al.[39]

Glass alteration layer pore depth analysis via positron annihilation spectroscopy

Positron annihilation spectroscopy (PAS) was utilized to analyze the open volume of glass alteration layers as a function of depth by observing energy distribution profiles after implantation of positrons. The incident kinetic energy of the positions determine the mean depth of the implantation profile.[44] A parameter related to the energy distribution known as the *R* parameter is used to qualitatively determine open volume (without differentiating between pore size and porosity) where a larger *R* value corresponds to more open volume. Methods and Supplementary Methods provide further details.

Figure 2a shows *R* parameters for UG, 3I7, 5I7, 7I7, 9I7, and 11I7 as a function of implantation energy in keV. In addition, Fig. 2a shows schematic descriptions of sample cross sections for 7I7, 9I7, and 11I7 scaled as a function of implantation energies calculated (see Methods for equation) using thicknesses measured on SEM images and calculated apparent density (ρ_{app}) values found in Supplementary Results. Figure 2b is a highlighted portion of Fig. 2a which shows low *R* values of UG, 3I7, 5I7, and 7I7 up to 70 keV and schematic descriptions of 3I7, 5I7, and 7I7 calculated similarly to the schematic descriptions in Fig. 2a. For implantation depths near the surface (<1 keV) positrons form positroniums (Ps) that escape into the vacuum of the beam line. The *R* values are high, and large surface defects may be visible (see Supplementary Methods for more details). UG shows a stable *R* value near 0 for all implantation energies >1 keV (i.e., at mean depths from 0.2 to 14 μm for 1 and 70 keV, respectively), indicating UG is homogenous throughout the whole sample and has no porosity above the detection limit (1% pore volume for this material). In Fig. 2a, *R* values for 9I7 and 11I7 reach their maximum in the AL, and their minimum in the UG portions. In 9I7, the *R* value is lower near the surface, suggesting partially blocked or constricted voids and no connection to the vacuum surface. Figure 2b shows that 7I7 has higher *R* values near the surface of the sample with a decrease until around 4 keV where it stabilizes near 0.015. At ~10 keV (near the AL/UG boundary), the *R* values decrease below the detection limit. The fluctuations of *R* at >10 keV for sample 3I7 and 5I7 are postulated to be a result of statistics and systematic effects of the positron beam and not buried porosity in the sample due to small-angle scattering of annihilation photons in the sample.

As discussed in Reiser et al.,[44] the depth resolution of PAS analysis decreases as energy increases, thereby leading to large transition zones between AL and UG (10–25 keV for 9I7 and 11I7). The higher pore volumes for 9I7 and 11I7 can be attributed to the dissolution of the glass network at higher pH due to increases in solubility for elements such as Si and Al. In addition, the increased porosity observed near the surface for 7I7 reflects structural changes in the alteration layer due to the rise in pH over the course of the experiment (see Table 1).

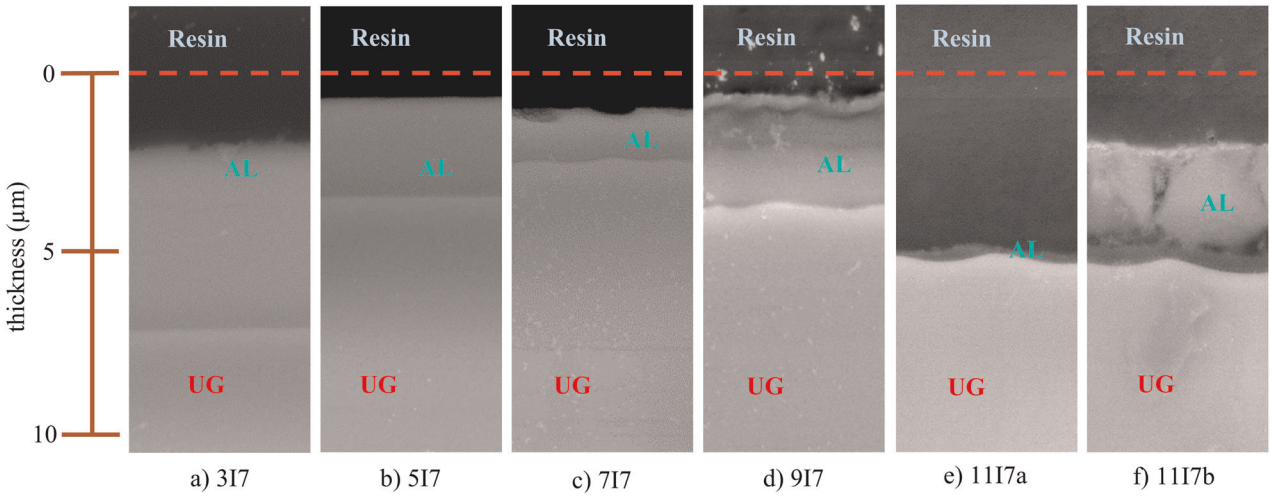

Fig. 1 Backscattered electron (BSE) SEM images of cross-sectioned samples. Images of samples include (**a**) 3I7, (**b**) 5I7, (**c**) 7I7, (**d**) 9I7, (**e**) 11I7a which shows a small conformal AL visible in the majority (>50%) of the surface analyzed, and (**f**) 11I7b which shows large fragile alteration products in addition to the small AL in the minority (<50%) of surface analyzed. Dashed line represents initial glass surface according to solution data (ETH_B).

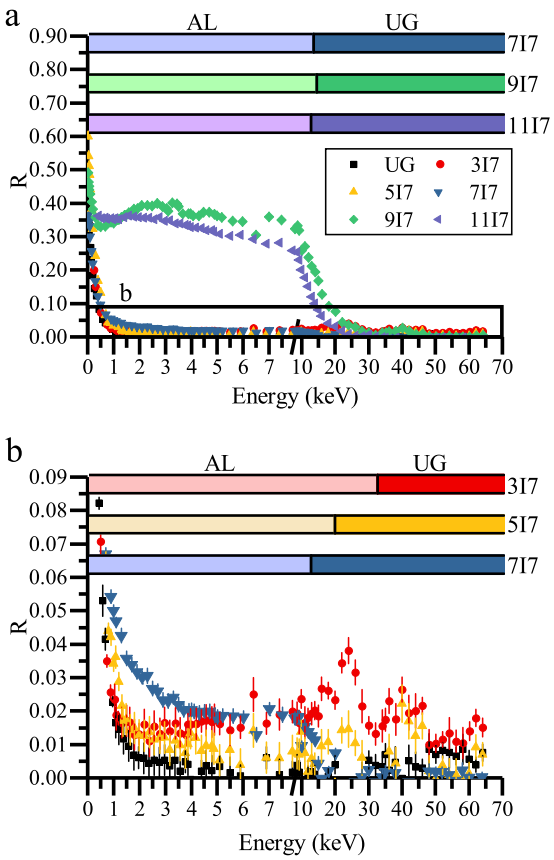

Fig. 2 *R* values as a function of energy up to 70 keV for altered glass samples. Results for (**a**) UG, 3I7, 5I7, 7I7, 9I7, and 11I7 are shown with schematic descriptions of 7I7, 9I7, and 11I7 and an enlarged portion of the same plot featuring (**b**) UG, 3I7, 5I7, and 7I7 and schematic descriptions for 3I7, 5I7, and 7I7.

Sample 9I7 shows less pore volume near the surface compared with the rest of the AL. These observations are consistent with experimental results and Monte–Carlo simulations of alteration layer structural formations of glasses similar to ISG altered in water.[45–47] However, 11I7 shows the reverse of this trend in that the AL contains the highest pore volumes near the surface and contains less pore volume deeper in the AL. The decrease in pore volume for 11I7 can be attributed to either inhomogeneity across the bulk AL or the solubility of Si at very high pH values.

The transition from the high *R* values at the surface to the nearly flat value in the alteration layers indicates that the voids are isolated and not interconnected. Interconnected porosity with a link to the vacuum surface render this transition more gradual with increased interconnection depth. The most gradual transition occurs in sample 7I7 with a characteristic depth energy of about 2 keV in Fig. 2b.

SAXS analysis

Figure 3a shows the results for 3I7, 5I7, 7I7, 9I7, and 11I7 with the power-law slope (*P*) values and radius of gyration (R_g) locations shown. For the model employed in this work, the *P* parameter describes the fractal dimension of the ensemble of scattering objects. P values near −4 indicate structures with smooth surfaces, *P* values between −3 and −4 indicate rough surfaces, and *P* values between −1 and −3 indicate mass fractals.[48] The R_g parameters characterize the size of the scattering objects regardless of shape.[48] All errors for *P* values presented in Fig. 3a are 0.2 or less. Table 2 shows the R_g fitted to the SAXS profiles for 3I7, 5I7, 7I7, 9I7, and 11I7 in Fig. 3a. Errors for large R_g values (>800 Å) are reported as two standard deviations of fits of multiple replicates of the each sample. Errors for small R_g (<100 Å) are estimated by comparing results of multiple uncertainty analysis methods available in the SAXS analysis software and choosing the largest realistic error.[49] Three intensity profiles are provided for 9I7 because the multiple replicates were not reproducible for *q* values < 0.005 $Å^{-1}$. The dip near 0.003 $Å^{-1}$ is an artifact due to data corrections resulting in over-subtraction of background in this area of weak scattering.

Samples 3I7, 5I7, 7I7, and 11I7 show increased scattering as evidenced by R_g knees in the low *q* region. The low pore volumes of 3I7, 5I7, and 7I7 (Table 2) and the increased scattering only in the low *q* regions imply most of the AL structure is well connected, and that phase changes from skeletal to pore structures is only visible at low *q*. Pores of the magnitude of R_g values (>1000 Å) for 3I7, 5I7, and 7I7 are surface defects in the AL (see Supplementary Fig. 1). 11I7 also shows increased scattering in this region, but the source of the scattering is not as evident. Based on Table 2, the minority phase is solid material (AL) (see Supplementary Methods

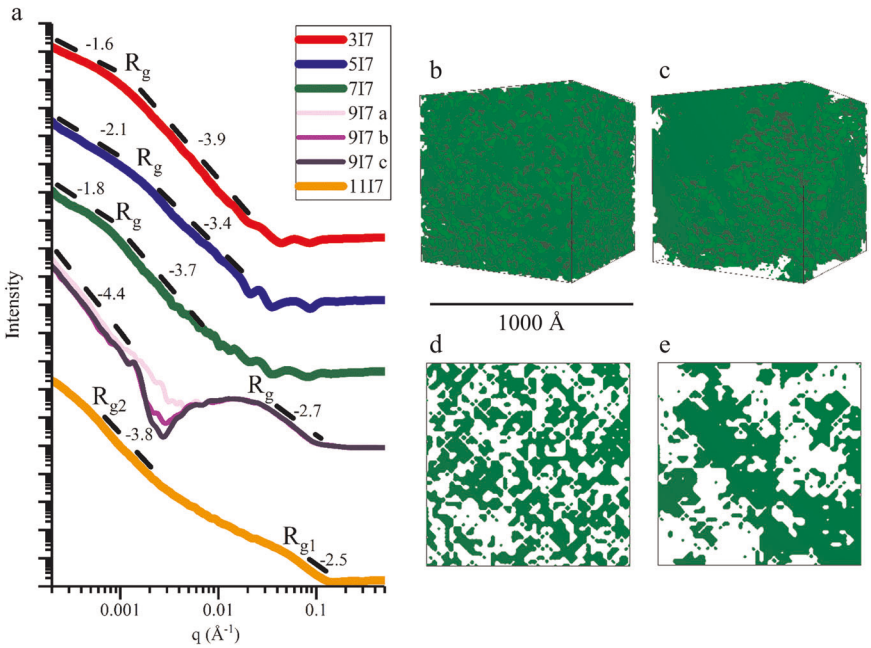

Fig. 3 SAXS intensity plot for altered glass samples and SAXSMorph representations. Plots are shown for (**a**) 3I7, 5I7, 7I7, 9I7, and 11I7 with scaled intensities for comparisons. The intensity line thicknesses indicate errors in scattering intensity from multiple replicates. The scattering profiles of all 9I7 analyses are shown since portions of the profiles are inconsistent with one another. Three-dimensional SAXSMorph representations of (**b**) 9I7 and (**c**) 11I7 and two-dimensional cross sections for (**d**) 9I7 and (**e**) 11I7, all with dimensions of 1000 Å (100 nm). Green represents solid material whereas white represents pores.

Table 2. Pore fractions and R_g values of synthetic aerogels SG-3, SG-7, SG-9 and alteration layers from 3I7, 5I7, 7I7, 9I7, and 11I7.

Sample	Pore fraction	R_{g1} (Å)	R_{g2} (Å)
SG-3	0.81 ± 0.08	8 ± 1	74 ± 2
SG-7	0.83 ± 0.08	16 ± 2	NA
SG-9	0.79 ± 0.08	15 ± 4	430 ± 40
3I7	0.21 ± 0.02	1900 ± 600	NA
5I7	0.23 ± 0.02	1180 ± 60	NA
7I7	0.31 ± 0.02	3400 ± 300	NA
9I7	0.50 ± 0.02	53 ± 3	NA
11I7	0.64 ± 0.02	37 ± 3	9900 ± 400

Pore fractions were determined in Reiser et al. (synthetic aerogels) and Kaspar et al. (glass alteration layers).[39,50]

for further discussion). Based on SEM micrographs, surface defects are not as prevalent for 11I7 as large pores are mostly present in the fragile portions of the alteration layer (see Fig. 1). The increased scattering for 11I7 at low q could be caused by the large pores in the fragile portions, but it could also be caused by some large structural artifact of the AL or a combination of both features.

Between 0.01 and 0.10 $Å^{-1}$, 9I7 and 11I7 show increased scattering with the presence of R_g knee behavior in Fig. 3a, whereas the others samples do not. The intensity profile of 7I7 shows a scattering artifact in the same region that could indicate the start of similar structural features as 9I7 and 11I7 which is plausible considering the increase in solution pH over the course of the experiment. The slopes of 9I7 and 11I7 in high-q regions only continues for a few decades, hence their P values may be not be trustworthy as their signals are lost to the background. Therefore, the P values likely could approach −4.

Figure 3b–e shows three-dimensional (3D) representations for (b) 9I7 and (c) 11I7 and two-dimensional (2D) cross sections for (d) 9I7 and (e) 11I7. The 3D structures are created from possible solutions to SAXS intensity profiles and are similar to the true structure. However, defined parameters and assumptions were made to construct the structures which are discussed in the section "Small-angle X-ray scattering". These assumptions resulted in smallest features being eliminated or smoothed out, causing the pores to appear more rounded and larger than they may be. The particles for 11I7 are significantly more varied in size with some particles much larger than those in 9I7. This observation corresponds with the SAXS profiles observed in Fig. 3a and shows increased scattering for 11I7 at lower q values in comparison to 9I7.

Figure 4a gives the SAXS results for the synthesized aerogels, again with P values (errors are 0.2 or less as before) and R_g locations indicated. The aerogel samples are denoted as SG-3, SG-7, and SG-9 for aerogels made at pH 3, 7, and 9. (In Reiser et al., these samples are referred to as ISG.3.B-15, ISG.7.A-60, and ISG.9.B-45, respectively.[50]) Table 2 shows the R_g fitted to the SAXS profiles for SG-3, SG-7, and SG-9. Errors for all R_g values are reported as two standard derivations of fits of multiple replicates of the each sample as fitting errors were less than the errors associated with replicates.

SG-3, SG-7, and SG-9 have similar scattering behavior in the high-q regions, showing faint R_{g1} knees (which may represent small dimer or trimer species) with changes in P values at the highest q region after the R_{g1} knees. The sizes of the primary particles of SG-3 and SG-9 vary as indicated by the R_{g2} values in Fig. 4a. SG-3 and SG-9 each have distinct R_g knees. In the q range lower than R_{g2} values for SG-3 and SG-9, both samples show a shelf, indicating that the R_{g2} represents the maximum particle size in that q region. Since SG-7 does not exhibit this shelf and has a

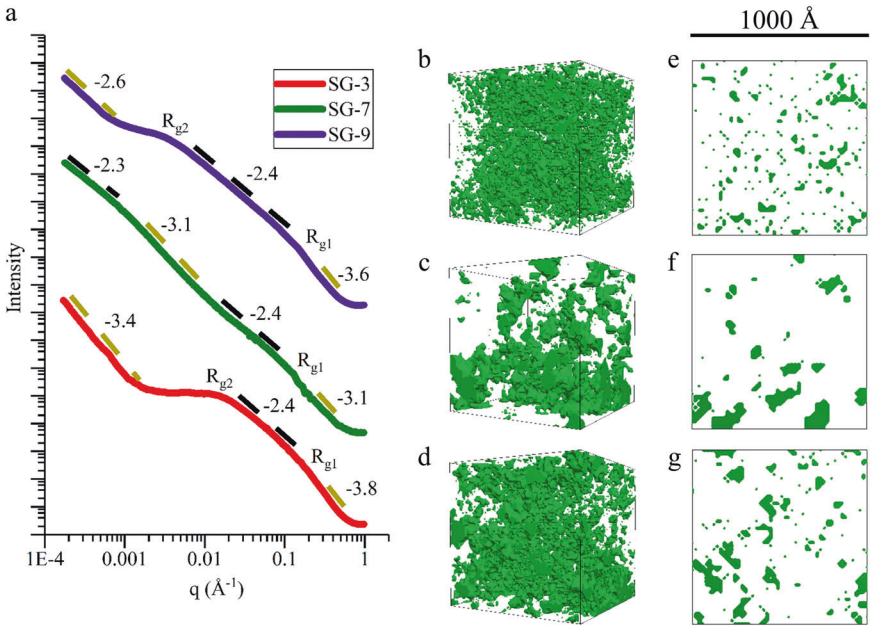

Fig. 4 SAXS intensity plot for synthetic aerogels and SAXSMorph representations. Plots are shown for (**a**) SG-3, SG-7, and SG-9 with scaled intensities for comparisons. The intensity line thicknesses indicate errors in scattering intensity from multiple replicates. Three-dimensional SAXSMorph representations of (**b**) SG-3, (**c**) SG-7, and (**d**) SG-9 and 2D cross sections for (**e**) SG-3, (**f**) SG-7, and (**g**) SG-9, all with dimensions of 100 nm (1000 Å). Green represents solid material whereas white represents pores.

fairly washed out R_{g2} knee, the primary particles in SG-7 vary greatly in sizes across several decades of q. The P values in the lowest q region of Fig. 4a indicate that larger primary particles are either rough surfaces, mass fractals, or primary particle sizes that vary across several orders of magnitude.

Figure 4 shows 3D representations of synthetic aerogels (b) SG-3, (c) SG-7, and (d) SG-9 and 2D cross sections of the same samples (e–g). The maximum sized primary particles of SG-3 are smaller than the largest particles seen for SG-7 and SG-9 that are consistent with that provided in Fig. 4 and Table 2. SG-7 contains increased scattering in Fig. 4 across a large range of q which is evident with the large variation in particle size seen in Fig. 4f.

STEM analysis of selected alteration layers

Figure 5 presents STEM annular darkfield images of prepared portions of (a) 9I7 and (b) 11I7 that are representative of the alteration layers seen in Fig. 1d, e. Figure 5c, d shows magnified portions of regions indicated on Fig. 5a, b. Samples 9I7 and 11I7 were chosen for STEM analysis after observing increased porosity with PAS and smaller structural features with SAXS in comparison to the other altered glass samples. Figure 5a shows multiple sub-layers within the alteration layer (AL-1, AL-2, AL-3) that have been observed by others under various experiments conditions.[10–12,18,44] The contrast in Fig. 5 shows that the alteration layer of 11I7 is more porous than 9I7. Figure 5d indicates the presence of porous channels connecting the surface of the alteration layer to the unaltered glass interface. This is more clearly illustrated in the GIF file of multiple STEM images taken at consecutive angles featured in Supplementary Video 1. A denser region in the alteration layer is observed in Fig. 5d. This could be a remnant of the large portion of the alteration layer observed in Fig. 1e likely lost during sample preparation.

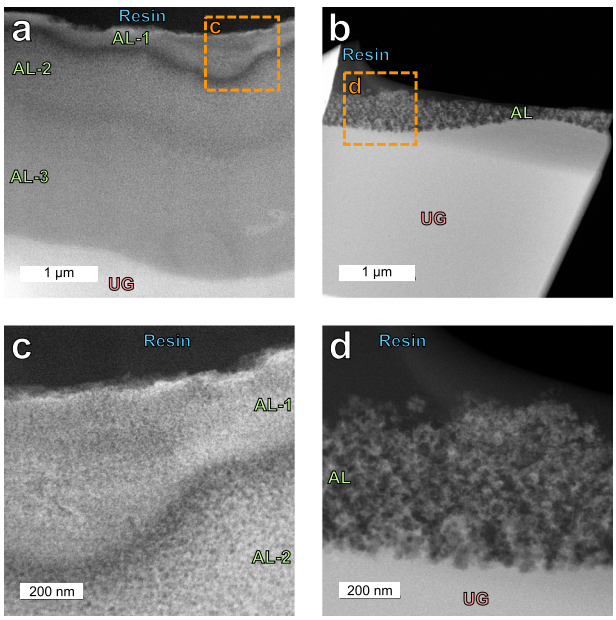

Fig. 5 STEM darkfield images of prepared portions of altered glass samples. Images of (**a**) 9I7 and (**b**) 11I7 are shown and magnified regions for (**c**) 9I7 and (**d**) 11I7 are indicated on (**a**) and (**b**). Unaltered glass is indicated as UG and alteration layers are indicated by AL.

DISCUSSION

In this study, the data from multiple characterization techniques utilized to probe the physical microstructure and morphology of glass alteration layers agree with one another. The STEM images in Fig. 5 compliment the SAXS data and modeling, especially for 11I7. In this study, SAXS was not able to differentiate between the multiple layers, thus the SAXS modeling provides data for the alteration layers as a homogenous amalgamation of the multiple layers (especially for 9I7). However, PAS was able to differentiate between these layers for 9I7 by providing physical evidence that alteration layers formed at pH 9 are denser near the surface (AL-1 in Fig. 5c) than the rest of the altered portion of the sample. This observation is in agreement with computational simulations of

structural formation of alteration layers in glasses similar to ISG in water[45–47] and previous experimental work.[10] Due to the denser portion of the alteration layer, diffusion of water and soluble ions through the alteration layer to unaltered glass could be reduced, thus causing glass alteration to decrease.

In regard to the synthetic aerogels, SG-3 was shown to contain smaller structural features in comparison to the structures in SG-9, which is similar to the observations seen for pure silica gels synthesized under various pH conditions.[19,20,22,26–28] The synthetic aerogels have larger pore fractions compared with 9I7 and 11I7 that impacts the connectivity of the primary particles into a formal structure. As a result, Rg impacts on the synthetic aerogels are easier to see in the computer-generated representations than for 9I7 and 11I7. No large structures (>100 Å) with distinct sizes were discernable for 9I7, whereas SG-9 shows evidence of large structures of distinct sizes. SG-3 also shows evidence of structures of distinct sizes closer to 9I7, but was created at a much lower pH. SG-7 and 11I7 show evidence of large structures as the sizes of the structures vary across several decades. The structure and porosity of the aerogels are dependent on several synthesis conditions, some of which were quite different from the conditions associated with the formation of the glass alteration layers. Specifically, the synthesis temperature for the aerogels was significantly lower than the temperature at which the alteration layers formed (room temperature vs. 90 °C). Previous work has shown that silica forms fewer but larger polymers as temperature increases,[51] implying that the structures formed for the aerogels may have been larger at higher synthesis temperatures.

Skeletal structural information determined for alteration layers at pH 9 and 11 and synthetic aerogels provide several indications of probable formation mechanisms of the alteration layers. For silica–water systems, higher silica solubility at high pH would result in larger pores as more material is removed into the bulk solution. Given the observed physical stability of the gel, it is probable that larger gel structures are present to compensate the large pores and maintain structural integrity. This is corroborated by the increasing stability of large silica particles and Ostwald ripening becoming more favorable as pH increases, both of which imply that larger gel structures are likely to exist at higher pH.[19] In addition, gels formed at pH 9 are expected to form quicker than gels formed at pH 11 due to the increased stability of silica particles as observed on silica sols by Iler.[19] Faster condensation rates for gels formed at pH 9 would lead to finer gel structure than gels formed at pH 11 which is supported by observations in Fig. 5c. While these explanations explain the differences in gel structures of 9I7 and 11I7, they do not explain why the structures are not more similar to the synthetic aerogels.

Unlike sol-gel derived aerogels which are formed from originally completely dissolved species (TEOS), the available Si species for gel formation in glass alteration layers may not be totally dissociated from the glass (non-Q^0 species). This is supported by previous experiments.[16,52] Fig. 6 shows speculative Si Q^n speciation on altered glass surfaces before the alteration layer forms for a) 9I7 and c) 11I7, where the Q^n species refers to the number of bonds connected to another network cation through a bridging oxygen atom. For example, Q^4 refers to Si atoms that have four bonds to oxygen atoms that are bonded to the atoms within the network structure (bridging oxygens) and Q^0 refers to Si that contain zero bonds to oxygen atoms bonded to the network structure (non-bridging oxygens). While the structures suggested in Fig. 6 are speculative, more Q^0 species are expected for 11I7 as seen as in Fig. 6c compared with the Q^0 speciation seen Fig. 6a for 9I7 due to the increased solubility of silica at higher pH.

For simple silica–water systems in basic conditions with low salt concentrations (similar to conditions during the formation of 9I7 and 11I7 glass alteration layers), silica gels form from aggregation of larger individual particles that have undergone significant Ostwald ripening before aggregation as opposed to immediate

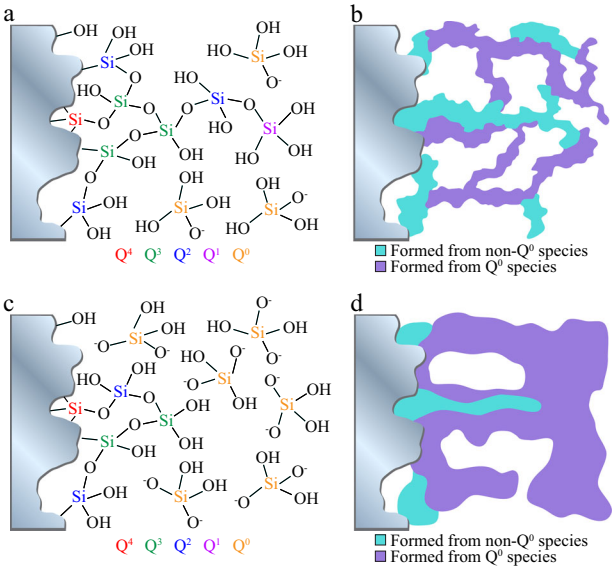

Fig. 6 Alteration layer formation schematics. At pH 9, (**a**) possible Si Q speciation on altered glass surfaces is shown while (**b**) shows plausible alteration layer gel structures formed from non-Q^0 species and Q^0 species in the immediate vicinity. Alteration layer formation schematics at pH 11 show (**c**) possible Si Q speciation on altered glass surfaces and (**d**) plausible alteration layer gel structures formed from non-Q^0 species and Q^0 species in the immediate vicinity.

aggregation of available small silica species. Q^0 species are available to completely participate in Ostwald ripening so the sizes of the gel structures are directly related to the concentration of Q^0 in the nearby solution. The gel structure sizes are dramatically reduced when the concentration of Q^0 species is low and most of the material is formed by the reconstruction of non-Q^0 units still connected to the glass. Based on the SAXS data in Fig. 3 and STEM images in Fig. 5, a schematic was developed (Fig. 6) to illustrate the various processes leading to the different alteration layer gel structures observed for (b) 9I7 and (d) 11I7, relative to the prevalence of non-Q^0 species and Q^0 species in the immediate vicinity. Due to a relative shortage of Q^0 species at pH 9, gel structures remain small (<100 Å) rather than grow into larger structures (>100 Å) as seen for synthetic aerogels at pH 9. Because more Q^0 species are available for Ostwald ripening at pH 11, larger structures in glass alteration layers are expected for 11I7 as seen in Fig. 6d.

The proposed formation model in Fig. 6 offers new insights into previous works. Gin et al. demonstrate that ISG altered in isotopically tagged silica saturated solution at pH 7 and pH 9 showed only slight enrichment of tagged Si originally from solution in the interior of the alteration layer, implying the alteration layer is composed mostly by silica originally from the glass.[16,37,52] By using solutions that are already saturated with respect to silica, fewer completely dissolved Si species would be available to participate in alteration layer formation compared with dilute solutions. As a result, the alteration layer is expected to form from mostly partially dissolved species and make a finer gel structure with smaller pores. Another Si isotope study experiment performed in initially dilute conditions, found porous alteration layers composed of Si originally from the isotopically tagged glass coupon and Si dissolved from a non-isotopically tagged coupon located in the same reactor.[11] The final pH values of the solutions in this study were greater than pH 10 which created conditions suitable for more soluble Si species to exist. The increased pH and the isotope results imply that the porous alteration layer was likely composed of primarily dissolved Si species (Q^0) as proposed in Fig. 6d.

While alteration layers of ISG formed in initially dilute solutions of various pH were analyzed in this work, Fournier et al. conducted a similar study using ISG in initially silica saturated solutions.[53] In their work, experiments were performed at higher S/V ratios for longer durations, but observed similar alteration behavior from $pH_{90\,°C}$ 1 to 11.[53] The analysis performed after 7 days of alteration in this work at lower S/V is relevant to long-term glass alteration, although some specific processes can only be captured with longer reaction times such as in Fournier et al. (secondary phase precipitation, alteration layer evolution with time, etc.)[53].

In this study, pore volumes and gel structures of alteration layers of glasses altered in dilute solutions of various pH values were investigated and compared with sol-gel synthesized aerogels with custom compositions based on alteration layer compositions. Glasses altered at higher pH values (9I7 and 11I7) were found to have more pore volume in the alteration layers in comparison to the other glass samples via PAS analysis. PAS also showed that 9I7 contained the least amount of pore volume near the surface and then had more pore volume in the interior of the alteration layer. SG-3 produced smaller skeletal structures than SG-7 and SG-9, and 9I7 produced smaller skeletal structures than 11I7. The results indicate that after 7 days, 11I7 was created in conditions similar to aerogels synthesized at neutral and high pH values, but 9I7 was likely not.

These findings imply that the solubility of silica is a major variable to consider in the formation of alteration layers. When Si solubility is high (as it is at pH 11), the completely dissociated Si species form the majority of the alteration layer as structures similar to those predicted by Iler for silica–water systems.[19] As solubility decreases and fewer completely dissolved Si species are present in solution, the alteration layer may form from a combination of partially dissolved species and completely dissolved species with structures less similar to synthetic aerogels and structures predicted by Iler.[19]

METHODS

Glass alteration experiments

The glass alteration samples described here have been used in a previous study.[39] The glass used for this study was the International Simple Glass (ISG).[3] The composition of ISG is found in Supplementary Table 1. Each experiment consisted of one ISG coupon (10 mm × 10 mm × 1 mm) that had been polished to a 250-nm finish with diamond paste (Ted Pella) on each face. Buffered reaction solutions were made to pH values 3, 5, 7, 9, and 11 (±0.2) at 90 °C. Specific details pertaining to solution preparations are presented in Supplementary Methods. Coupons were inserted into Savillex® vials containing 10 mL of the pH-adjusted solutions to obtain a glass-surface-area-to-solution-volume ratio (*S/V*) of 25 m^{-1}. Experiments were conducted in an oven heated to 90 °C for 7 days without disturbing the samples. At the conclusion of the alteration experiments, the solutions were removed and the glass coupons were washed and immersed with ethanol. The ethanol was then exchanged with liquid CO_2, and the glass samples were dried using supercritical CO_2 to preserve the structure of any porous alteration layer that may have formed. The final pH values of the solutions were measured at 90 °C and can be found in Table 1.

Sol-gel experiments

The syntheses processes of the sol-gel-derived silicate aerogels are described in more detail elsewhere.[50] In brief, aerogels were synthesized at room temperature using compositions comparable to those of altered 3I7, 7I7, and 9I7 listed in Supplementary Table 1. TEOS (Aldrich®), deionized water (H_2O), and ethanol were mixed in a molar ratio of 1:4:8. Other components of the sol-gel included aluminum-tri-*sec*-butoxide (Aldrich®), zirconium(IV) propoxide (Acros Organics®), sodium ethoxide (Sigma-Aldrich®), and calcium 2-methoxyethoxide (Gelest, Inc.). The pH of each mixture was adjusted after adding the TEOS, with 0.1 M HNO_3 to reach pH 3, a mixture of 2.7 M NH_4OH and 0.4 M NH_4F (NH_4OH/NH_4F) for pH 7 (http://www.aerogel.org/), and concentrated NH_4OH or NH_4OH/NH_4F for pH 9. After the samples had gelled, they were immersed in ethanol and the solvent was renewed at least ten times to ensure that all mobile species were removed. Liquid CO_2 was then exchanged with ethanol thoroughly before the samples were supercritically dried to prevent the gel structures from collapsing.

Inductively coupled plasma optical emission spectrometry

Aliquots of altered glass leachate solutions were diluted with 0.1–0.3 mol·L^{-1} HNO_3 and analyzed using inductively coupled plasma optical emission spectrometry (ICP-OES) for Al, B, Ca, K, Na, Si, and Zr with a PerkinElmer Optima® 8300 dual view spectrometer with an Elemental Scientific SC4 DX *FAST* auto-sampler interface. The instrument was calibrated using standards (High-Purity Standards Corporation) to generate calibration curves with a range of 50 ppb–50 ppm. Calibration verifications were performed as required for the Hanford Analytical Quality Assurance Requirements Document.[54] Calibration blanks were analyzed after each calibration verification, and the calibration was independently verified using standards made by Inorganic Ventures®. Concentrations were determined and used to calculate the composition of alteration layers and synthetic aerogels and equivalent alteration layer thicknesses. See Supplementary Methods for calculation explanations.

Scanning electron microscopy

Dried portions of the altered coupons were embedded into epoxy resin (Epoxy Set, Allied High Tech Products, Inc.), sectioned to expose a cross section, and then polished to 0.03 µm with colloidal silica in preparation for scanning electron microscopy (SEM) analysis. A JSM 7001 F (JEOL, Ltd.) equipped with a field emission gun was used. Alteration layer thicknesses were measured using backscattered electron (BSE) SEM images of altered sample cross sections and ImageJ software greyscale analysis. Alteration layer thicknesses were measured at multiple points (>50) to improve the accuracy and reproducibility of the results.

Positron annihilation spectroscopy

Glass surfaces were analyzed using positron annihilation spectroscopy (PAS) at Washington State University to investigate open volume within the structures of various alteration layers and unaltered ISG (UG). Analysis conditions were identical to conditions described in Reiser et al.[44] For this study, ratios of 3- to 2 γ annihilation events (*R* parameter) were evaluated. Resulting *R* values were normalized to the UG value and adjusted so the *R* value of UG is zero and higher *R* values imply that the sample contains more open volume than UG. See Supplementary Methods for further explanation on the *R* parameter.

The mean implantation depth (*D*, nm) is related to the incident kinetic energy (*E*, keV) and apparent density of the material (ρ_{app}, g·cm^{-3}) by the empirical formula given in Eq. (1):[44,55–57]

$$D = \left(\frac{40}{\rho_{app}}\right) E^{1.6} \quad (1)$$

where small variances in material composition, surface roughness, and very large pore volume fractions are systematic sources of error. The quantity of open volume as a function of depth into the sample can be inferred by analyzing *R* parameters as implantation energy increases, as higher energy positrons penetrate deeper on average into a solid before annihilating.

Small-angle X-ray scattering

Altered glass and gel samples were analyzed using ultra-small-angle X-ray scattering (USAXS) and small-angle X-ray scattering (SAXS) experiments conducted at the Advanced Photon Source (Argonne National Laboratory, Lemont, IL, USA) on beamline 9-ID, station C. The setup is described elsewhere.[58,59] The analysis conditions for this particular analysis is described in Reiser et al.[50] Based on the pore fractions presented in Table 2, SAXS analyzes the skeletal phase of the synthetic aerogels as pore fractions are >80% (see Reiser et al.[50]). For alteration layers on 3I7, 5I7, and 7I7, pore fractions are <50%, indicating the SAXS data measured intensities from mainly the skeletal phase, but also pores. Likewise, the SAXS data for 11I7 is influenced by solid material more than pores due to its pore fraction. The pore fraction for 9I7 is ca. 50%, implying an equal contribution of both phases in the SAXS scattering data. See Supplementary Methods for further explanation.

The samples were analyzed using the unified method developed by Beaucage and Schafer.[60,61] The radius of gyration (R_g) and power-law exponent (*P*) parameters were of particular interest in this study and are described in more detail in Reiser et al.[50]

SAXSMorph was used to generate three-dimensional representations (cubes) of structures within 9I7, 11I7, SG-3, SG-7, and SG-9, using known pore fractions (see Table 2) and SAXS profiles.[62] The structures created are random examples that fit the SAXS data which are similar to the true structures. Dimensions of the constructed cubes were defined to be 1000 Å (100 nm); input minimum and maximum q values were 0.008–0.1 $Å^{-1}$ for 9I7, 0.0006–0.1 $Å^{-1}$ for 11I7, and 0.0006–0.7 $Å^{-1}$ for SG-3, SG-7, and SG-9. Minimum and maximum q values were chosen to include all relevant features seen on SAXS plots down to 0.0006 $Å^{-1}$. Persistence of vision (POV) free software is used to visualize the representations.[63] The samples in this study fit all of the requirements with the exception of high q values must approach a power-law slope of −4 in all samples, which is not the case for 9I7 and 11I7. This issue is addressed in the section "SAXS analysis". The largest consequence of having power-law slopes greater than −4 is that the smallest features are smoothed out in the generated structure more than the actual structure.

Scanning transmission electron microscopy

STEM specimen preparation of samples 9I7 and 11I7 was performed using an FEI Helios dual-beam focused ion beam/scanning electron microscope (FIB/SEM). Conventional liftout procedures[1] were performed to extract a ~15-µm long and 8-µm tall section from an epoxy mounted and polished cross section of the corroded glass surface previously prepared for SEM analysis (see the section "Scanning electron microscopy"). The surface was protected by a bilayer of e-beam and i-beam deposited Pt prior to FIB milling. The extracted portion extended from the epoxy embedding material, across the altered glass surface and into pristine glass. The FIB lamella was thinned to ~200 nm thickness with 30 kV Ga^+, and further thinned to <100 nm thickness using 2 kV Ga^+ to minimize beam damage to the sample. STEM darkfield imaging was performed on prepared 9I7 and 11I7 samples to estimate the level of porosity in the samples. Analytical electron microscopy was accomplished using a JEOL ARM 200 F cold field, aberration probe corrected STEM operated at 200 kV equipped with a JEOL Centurio EDS detector with a solid collection angle of 0.9 sR. Data analysis was completed using Gatan Microscopy Suite 3.0 and Noran Pathfinder software.

DATA AVAILABILITY

The authors declare the data supporting the findings of this study are available within the paper and its supplementary information files.

Received: 17 January 2019; Accepted: 16 December 2019;
Published online: 21 February 2020

REFERENCES

1. Donald, I. W. *Waste Immobilization in Glass and Ceramic Based Hosts* (John Wiley & Sons, Inc., 2010).
2. Ojovan, M. I. & Lee, W. E. Glassy wasteforms for nuclear waste immobilization. *Metall. Mater. Trans. A Phys. Metall. Mater. Sci.* **42**, 837–851 (2011).
3. Gin, S. et al. An international initiative on long-term behavior of high-level nuclear waste glass. *Mater. Today* **16**, 243–248 (2013).
4. Vienna, J. D., Ryan, J. V., Gin, S. & Inagaki, Y. Current understanding and remaining challenges in modeling long-term degradation of borosilicate nuclear waste glasses. *Int. J. Appl. Glas. Sci.* **4**, 283–294 (2013).
5. Gin, S. Open scientific questions about nuclear glass corrosion. *Procedia Mater. Sci.* **7**, 163–171 (2014).
6. Gin, S., Frugier, P., Jollivet, P., Bruguier, F. & Curti, E. New insight into the residual rate of borosilicate glasses: effect of s/v and glass composition. *Int. J. Appl. Glas. Sci.* **4**, 371–382 (2013).
7. Gin, S. et al. Long-term behavior of R7T7-type nuclear glass: current state of knowledge and outlook. *Mater. Res. Soc. Symponisum Proc.* **824**, 1–6 (2004).
8. Rebiscoul, D. et al. Morphological evolution of alteration layers formed during nuclear glass alteration: new evidence of a gel as a diffusive barrier. *J. Nucl. Mater.* **326**, 9–18 (2004).
9. Gin, S., Ryan, J. V., Schreiber, D. K., Neeway, J. & Cabié, M. Contribution of atom-probe tomography to a better understanding of glass alteration mechanisms: application to a nuclear glass specimen altered 25 years in a granitic environment. *Chem. Geol.* **349–350**, 99–109 (2013).
10. Dohmen, L. et al. Pattern formation in silicate glass corrosion zones. *Int. J. Appl. Glas. Sci.* **4**, 357–370 (2013).
11. Geisler, T. et al. The mechanism of borosilicate glass corrosion revisited. *Geochim. Cosmochim. Acta* **158**, 112–129 (2015).
12. Geisler, T. et al. Aqueous corrosion of borosilicate glass under acidic conditions: a new corrosion mechanism. *J. Non Cryst. Solids* **356**, 1458–1465 (2010).
13. Gin, S. et al. The controversial role of inter-diffusion in glass alteration. *Chem. Geol.* **440**, 115–123 (2016).
14. Gin, S. et al. Atom-Probe Tomography, TEM and ToF-SIMS study of borosilicate glass alteration rim: a multiscale approach to investigating rate-limiting mechanisms. *Geochim. Cosmochim. Acta* **202**, 57–76 (2017).
15. Doremus, R. H. Interdiffusion of hydrogen and alkali ions in a glass surface. *J. Non Cryst. Solids* **19**, 137–144 (1975).
16. Gin, S. et al. The fate of silicon during glass corrosion under alkaline conditions: a mechanistic and kinetic study with the International Simple Glass. *Geochim. Cosmochim. Acta* **151**, 68–85 (2015).
17. Hellmann, R. et al. Unifying natural and laboratory chemical weathering with interfacial dissolution–reprecipitation: a study based on the nanometer-scale chemistry of fluid–silicate interfaces. *Chem. Geol.* **294–295**, 203–216 (2012).
18. Hellmann, R. et al. Nanometre-scale evidence for interfacial dissolution–reprecipitation control of silicate glass corrosion. *Nat. Mater.* **14**, 307–311 (2015).
19. Iler, R. K. *The Chemistry of Silica: Solubility, Polymerization, Colloid and Surface Properties, and Biochemistry* (John Wiley & Sons, Inc. 1979).
20. Brinker, C. J. & Scherer, G. W. *Sol-Gel Science: The Physics and Chemistry of Sol-Gel Processing* (Academic Press, Inc. 1990).
21. Livage, J. & Sanchez, C. Sol-gel chemistry. *J. Non Cryst. Solids* **145**, 11–19 (1992).
22. Brinker, C. J. et al. Sol-gel transition in simple silicates II. *J. Non Cryst. Solids* **63**, 45–59 (1984).
23. Klein, L. C. Sol-gel processing of silicates. *Annu. Rev. Mater. Sci.* **15**, 227–248 (1985).
24. Soleimani Dorcheh, A. & Abbasi, M. H. Silica aerogel; synthesis, properties and characterization. *J. Mater. Process. Technol.* **199**, 10–26 (2008).
25. Barisik, M., Atalay, S., Beskok, A. & Qian, S. Size dependent surface charge properties of silica nanoparticles. *J. Phys. Chem. C.* **118**, 1836–1842 (2014).
26. Brinker, C. J., Roth, E. P., Scherer, G. W. & Tallant, D. R. Structural evolution during the gel to glass conversion. *J. Non Cryst. Solids* **71**, 171–185 (1985).
27. Buckley, A. & Greenblatt, M. The sol-gel preparation of silica gels. *J. Chem. Educ.* **71**, 599–602 (1994).
28. Brinker, C. J., Keefer, K. D., Roth, E. P., Schaefer, D. W. & Ashley, C. S. Sol-gel transition in simple silicates. *J. Non Cryst. Solids* **48**, 47–64 (1982).
29. Kaspar, T. C. et al. Physical and optical properties of the International Simple Glass. *npj Mater. Degrad.* **3**, 15 (2019).
30. Guerette, M. & Huang, L. In-situ Raman and Brillouin light scattering study of the international simple glass in response to temperature and pressure. *J. Non Cryst. Solids* **411**, 101–105 (2015).
31. Lenting, C. et al. Towards a unifying mechanistic model for silicate glass corrosion. *npj Mater. Degrad.* **2**, 1–10 (2018).
32. Lu, X., Deng, L., Kerisit, S. & Du, J. Structural role of ZrO_2 and its impact on properties of boroaluminosilicate nuclear waste glasses. *npj Mater. Degrad.* **2**, 19 (2018).
33. Inagaki, Y., Kikunaga, T., Idemitsu, K. & Arima, T. Initial dissolution rate of the International Simple Glass as a function of pH and temperature measured using microchannel flow-through test method. *Int. J. Appl. Glas. Sci.* **4**, 317–327 (2013).
34. Neeway, J. J., Rieke, P. C., Parruzot, B. P., Ryan, J. V. & Asmussen, R. M. The dissolution behavior of borosilicate glasses in far-from equilibrium conditions. *Geochim. Cosmochim. Acta* **226**, 132–148 (2018).
35. Abdelouas, A. et al. A preliminary investigation of the ISG glass vapor hydration. *Int. J. Appl. Glas. Sci.* **4**, 307–316 (2013).
36. Rieke, P. C., Kerisit, S., Ryan, J. V. & Neeway, J. J. Adaptation of the GRAAL model of Glass Reactivity to accommodate non-linear diffusivity. *J. Nucl. Mater.* **512**, 79–93 (2018).
37. Gin, S. et al. Dynamics of self-reorganization explains passivation of silicate glasses. *Nat. Commun.* **9**, 1–9 (2018).
38. Advocat, T., Crovisier, J. L. & Vernaz, E. Aqueous corrosion of French R7T7 nuclear waste glass: selective then congruent dissolution by pH increase. *Comptes Rendus - Acad. Des. Sci. Ser. II* **313**, 407–412 (1991).
39. Kaspar, T. C., Reiser, J. T., Ryan, J. V. & Wall, N. A. Non-destructive characterization of corroded glass surfaces by spectroscopic ellipsometry. *J. Non Cryst. Solids* **481**, 260–266 (2018).
40. Strachan, D. Glass dissolution as a function of pH and its implications for understanding mechanisms and future experiments. *Geochim. Cosmochim. Acta* **219**, 111–123 (2017).
41. Inagaki, Y. et al. Aqueous alteration of Japanese simulated waste glass P0798: effects of alteration-phase formation on alteration rate and cesium retention. *J. Nucl. Mater.* **354**, 171–184 (2006).
42. Inagaki, Y. et al. Initial dissolution rate of a Japanese simulated high-level waste glass P0798 as a function of pH and temperature measured by using microchannel flow-through test method. *J. Nucl. Sci. Technol.* **49**, 438–449 (2012).

43. Gislason, S. R. & Oelkers, E. H. Mechanism, rates, and consequences of basaltic glass dissolution: II. An experimental study of the dissolution rates of basaltic glass as a function of pH and temperature. *Geochim. Cosmochim. Acta* **67**, 3817–3832 (2003).
44. Reiser, J. T. et al. The use of positrons to survey alteration layers on synthetic nuclear waste glasses. *J. Nucl. Mater.* **490**, 75–84 (2017).
45. Cailleteau, C. et al. Insight into silicate-glass corrosion mechanisms. *Nat. Mater.* **7**, 978–983 (2008).
46. Cailleteau, C., Devreux, F., Spalla, O., Angeli, F. & Gin, S. Why do certain glasses with a high dissolution rate undergo a low degree of corrosion? *J. Phys. Chem. C.* **115**, 5846–5855 (2011).
47. Devreux, F., Ledieu, A., Barboux, P. & Minet, Y. Leaching of borosilicate glasses. II. Model and Monte-Carlo simulations. *J. Non Cryst. Solids* **343**, 13–25 (2004).
48. Roon, R. J. *Methods of X-Rays and Neutron Scattering in Polymer Science* (Oxford University Press, 2004).
49. Ilavsky, J. & Jemian, P. R. Irena: tool suite for modeling and analysis of small-angle scattering. *J. Appl. Crystallogr.* **42**, 347–353 (2009).
50. Reiser, J. T., Ryan, J. V. & Wall, N. A. Sol–gel synthesis and characterization of gels with compositions relevant to hydrated glass alteration layers. *ACS Omega* **4**, 16257–16269 (2019).
51. Rothbaum, H. P. & Rohde, A. G. Kinetics of silica polymerization and deposition from dilute solutions between 5 and 180 °C. *J. Colloid Interface Sci.* **71**, 533–559 (1979).
52. Gin, S. et al. Origin and consequences of silicate glass passivation by surface layers. *Nat. Commun.* **6**, 6360 (2015).
53. Fournier, M. et al. Effect of pH on the stability of passivating gel layers formed on International Simple Glass. *J. Nucl. Mater.* **524**, 21–38 (2019).
54. *Hanford Analytical Services Quality Assurance Requirements Document* Vol. 4 (2014).
55. Asoka-Kumar, P., Lynn, K. G. & Welch, D. O. Characterization of defects in Si and SiO_2-Si using positrons. *J. Appl. Phys.* **76**, 4935–4982 (1994).
56. Gidley, D. et al. Positronium annihilation in mesoporous thin films. *Phys. Rev. B* **60**, R5157–R5160 (1999).
57. Schultz, P. J. & Lynn, K. G. Interaction of positron beams with surfaces, thin films, and interfaces. *Rev. Mod. Phys.* **60**, 701–707 (1988).
58. Ilavsky, J. et al. Ultra-small-angle X-ray scattering at the Advanced Photon Source. *Appl. Crystallogr.* **42**, 469–479 (2009).
59. Ilavsky, J. et al. Ultra-small-angle X-ray scattering instrument at the advanced photon source: history, recent development, and current status. *Metall. Mater. Trans. A* **44A**, 68–76 (2012).
60. Beaucage, G. & Schaefer, D. W. Structural studies of complex systems using small-angle scattering: a unified Guinier/power-law approach. *J. Non-Crystalline Solids.* **172–174**, 797–805 (1994).
61. Beaucage, G. Approximations leading to a unified exponential/power-law approach to small-angle scattering. *J. Appl. Crystallogr.* **28**, 717–728 (1995).
62. Ingham, B., Li, H., Allen, E. L. & Toney, M. F. SAXSMorph: a program for generating representative morphologies for two-phase materials from small-angle X-ray and neutron scattering data. *J. Appl. Crystallogr.* **44**, 221–224 (2011).
63. The Persistence of Vision Pty. Ltd., https://doi.org/10.2307/115995 (2018).

ACKNOWLEDGEMENTS

This research used resources of the Advanced Photon Source, a U.S. Department of Energy (DOE) Office of Science User Facility operated for the DOE Office of Science by Argonne National Laboratory under Contract No. DE-AC02-06CH11357. The authors would like to thank Brian Riley, Jared Kroll, and Jacob Peterson for sol-gel synthesis assistance and Jarrod Crum with assistance with SEM analysis. The authors also express their gratitude to Benjamin Parruzot for his assistance with editing and formatting figures and general insight and feedback throughout this study. This work was jointly funded by the US Department of Energy Office of Nuclear Energy (Materials Recovery and Waste Form Development) and the Office of Environmental Management (Tank Waste Management, EM-21). Pacific Northwest National Laboratory is a multi-program national laboratory operated for the U.S. Department of Energy by Battelle Memorial Institute under Contract DE-AC06-76RLO 1830.

AUTHOR CONTRIBUTIONS

Experiments were designed by J.T.R. and J.V.R. and performed by J.T.R. M.H.W. collected PAS data and assisted with data analysis; J.I. assisted with SAXS collection and analysis; D.K.S. performed FIB liftout; and M.J.O. performed STEM imaging and assisted with analysis. J.T.R., J.V.R., and N.A.W. contributed to result interpretation. J.T.R. wrote the paper with inputs and editing from the other authors.

COMPETING INTERESTS

The authors declare no competing interests.

ADDITIONAL INFORMATION

Supplementary information is available for this paper at https://doi.org/10.1038/s41529-020-0109-y.

Correspondence and requests for materials should be addressed to J.V.R.

Reprints and permission information is available at http://www.nature.com/reprints

Publisher's note Springer Nature remains neutral with regard to jurisdictional claims in published maps and institutional affiliations.

Open Access This article is licensed under a Creative Commons Attribution 4.0 International License, which permits use, sharing, adaptation, distribution and reproduction in any medium or format, as long as you give appropriate credit to the original author(s) and the source, provide a link to the Creative Commons license, and indicate if changes were made. The images or other third party material in this article are included in the article's Creative Commons license, unless indicated otherwise in a credit line to the material. If material is not included in the article's Creative Commons license and your intended use is not permitted by statutory regulation or exceeds the permitted use, you will need to obtain permission directly from the copyright holder. To view a copy of this license, visit http://creativecommons.org/licenses/by/4.0/.

© The Author(s) 2020